ACS APPLIED OPTICAL MATERIALS

pubs.acs.org/acsaom

Article

Temperature-Dependent Linear and Quadratic Electroabsorption Spectra of Perovskite Nanocrystalline Films of $CH_3NH_3PbBr_3$

Shailesh Rana, Kamlesh Awasthi, Sudhakar Narra, Eric Wei-Guang Diau, and Nobuhiro Ohta*

Cite This: ACS Appl. Opt. Mater. 2025, 3, 2870−2882

Read Online

ACCESS | Metrics & More | Article Recommendations | Supporting Information

ABSTRACT: Electric field effects on exciton absorption in methylammonium lead tribromide ($MAPbBr_3$) nanocrystalline (NC) films were examined between 290 and 60 K using electroabsorption (EA) spectroscopy. Linear ($EA_{1\omega}$) and quadratic ($EA_{2\omega}$) spectra, scaling with field strength, were obtained for $MAPbBr_3$:NC films embedded between FTO/PMMA (Sample **A**) or TiO_2/PMMA (Sample **B**). Absorption and $EA_{2\omega}$ spectra of both samples were essentially identical at all temperatures, confirming that $EA_{2\omega}$ features reflect intrinsic $MAPbBr_3$:NC properties. From $EA_{2\omega}$ analysis, changes in electric dipole moment ($\Delta\boldsymbol{\mu}$) and polarizability ($\Delta\boldsymbol{\alpha}$) following exciton absorption, and exciton binding energy (E_B) were extracted and compared with $MAPbBr_3$ quantum dots. In contrast, $EA_{1\omega}$ spectra exhibited strong interface dependence, and the exciton absorption band showed pronounced polarity-dependent broadening and narrowing of exciton absorption band induced by application of electric field, except for Sample **B** at 60 K. These results indicate that $EA_{1\omega}$ arises from linear Stark shifts of excitons localized at the PMMA/NC and FTO (or TiO_2)/NC interfaces, with opposite field-induced spectral shifts at the two boundaries. Simulations reproduced the experimental spectra by assuming slightly different exciton peak positions at the interfaces and opposite Stark shifts under applied fields. Franz−Keldysh oscillations, characteristic of field-modulated continuum absorption, were also observed at 60 K in both $EA_{1\omega}$ and $EA_{2\omega}$ spectra, most prominently in the $EA_{1\omega}$ spectra of Sample **B**. These findings disentangle bulk and interfacial contributions to the EA response of $MAPbBr_3$:NC films and provide quantitative insights into exciton binding and field-induced effects in perovskite nanocrystals.

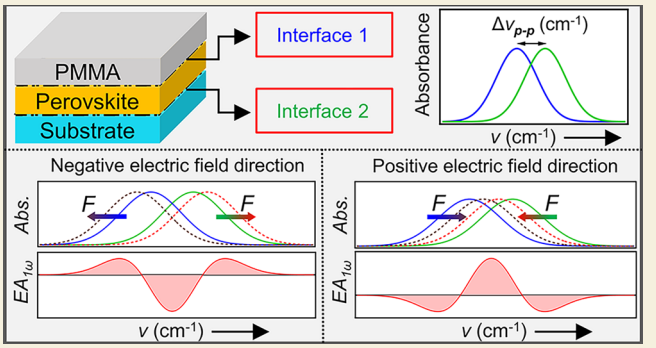

KEYWORDS: *elecrtoabsorption spectroscopy, perovskite nanocrystal, $MAPbBr_3$, interfacial linear Stark effect, quadratic Stark effect, Franz:Keldysh oscillation, electric dipole moment and polarizability*

INTRODUCTION

Hybrid organic−inorganic halide perovskites (OIHPs) are pioneering semiconducting materials due to their extraordinary photoelectronic attributes and aptitude for optoelectronic functionalities.[1−6] Despite their remarkable photoelectronic properties, there is a concern that ion migration and light illumination significantly affect their performance, i.e., a prolonged light illumination can accelerate ion migration, induce trap states, and trigger phase segregation, all of which enhance nonradiative recombination and degrade optical and charge transport properties.[7−11] Long-term stability is another significant concern for OIHPs in their journey toward practical applications. For instance, the operational stability of solar cells is often measured by the T_{80} metric—the time over which the power conversion efficiency drops to 80% of its initial value. For stable perovskite solar cells (PSCs), this value is typically in the range of a few hundred to a thousand hours under continuous illumination and standard testing conditions.[12,13] In contrast, silicon solar cells demonstrate a T_{80} lifetime of 40 years. This disparity highlights a key barrier to the commercial viability of perovskite photovoltaics, underscoring the need for improved material and device stability. Numerous efforts, such as compositional engineering, interface engineering, and incorporation of cross-linking agents, have been introduced to improve the intrinsic stability of the perovskite absorber layer.[14−19] From a fundamental perspective, it is equally important to comprehend the electronic properties of the perovskite absorbing layer in the bulk and at the interface in contact with another layer or substrate.

As our understanding of the bulk and interface properties of perovskite materials deepens, so does the need for advanced tools to explore their intricate optoelectronic features. In this context, electroabsorption (EA) spectroscopy has emerged as a

Received: September 18, 2025
Revised: November 9, 2025
Accepted: November 11, 2025
Published: November 21, 2025

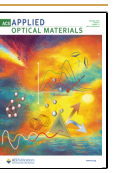

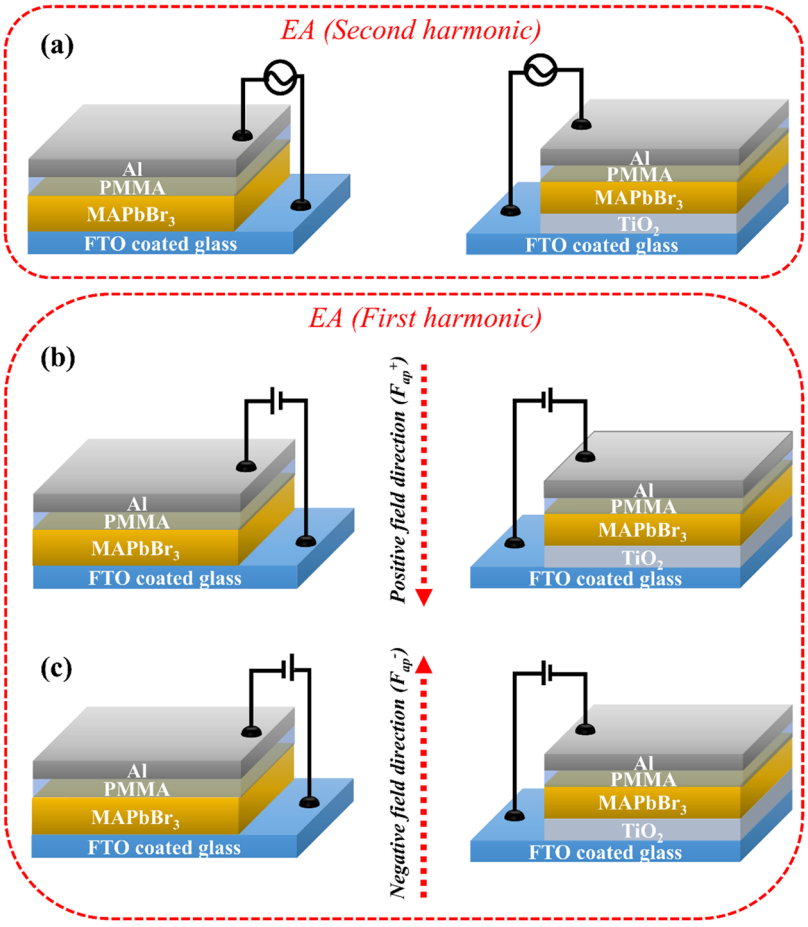

Figure 1. Schematic representation of $MAPbBr_3$:NC deposited on FTO (left, Sample **A**) and TiO_2 layer (right, Sample **B**) with PMMA overlayer for the measurements of $EA_{2\omega}$ spectra (a) and $EA_{1\omega}$ spectra (b, c), where the field-induced change in transmitted light intensity (ΔT_{EX}) synchronized at the second harmonic and first harmonic of the frequency of applied electric field (F_{ap}), respectively, was monitored. Here, the direction of F_{ap} from Al to FTO is a positive field direction (F_{ap}^{+}) (b), whereas the direction from FTO to Al is a negative field direction (F_{ap}^{-}) (c).

powerful technique, offering a comprehensive approach to the optoelectronic characterization of the perovskite family.[20−33] Particularly, EA signals obtained from the applied electric field (F_{ap})−induced change in absorption intensity synchronized at the second harmonic of the modulation frequency of the F_{ap}, $EA_{2\omega}$, provide valuable insights into the photophysics of excitons (E_X), including their binding energy and effective mass.[20−24] This technique has proven instrumental in investigating various features in OIHPs, such as ion migration, phase segregation, degradation mechanisms, charge carrier interactions, and dielectric confinement effects.[34−40]

We reported the $EA_{2\omega}$ spectra of the methylammonium lead tribromide ($MAPbBr_3$) nanocrystalline film deposited on the FTO at room temperature (***R-T***).[22] The $EA_{2\omega}$ spectra resulting from the Stark effect were analyzed by the integral method (***I-M***). The analysis led to the estimation of the change in electric dipole moment ($\Delta\boldsymbol{\mu}$) and polarizability ($\Delta\boldsymbol{\alpha}$) following photoexcitation into the E_X band and exciton binding energy (E_B) at ***R-T***, yielding values of 2.2 D, −4.1 Å^3, and 14.0 meV. We also observed $EA_{2\omega}$ spectra of $MAPbBr_3$ quantum dots ($MAPbBr_3$:QDs) doped in a PMMA film over a temperature (T) range of 290−40 K.[24] It was found that the intensity of the $EA_{2\omega}$ spectra of $MAPbBr_3$:QDs depended on the modulation frequency of the F_{ap}, particularly at low frequencies, reflecting the slow migration of ions. To avoid such ion migration effect, the $EA_{2\omega}$ spectra observed with F_{ap} having a high frequency of 1 kHz were analyzed, and the magnitudes of $\Delta\boldsymbol{\mu}$, $\Delta\boldsymbol{\alpha}$, and E_B of $MAPbBr_3$:QDs were estimated at various T. The extracted values of $\Delta\boldsymbol{\mu}$ and $\Delta\boldsymbol{\alpha}$ of $MAPbBr_3$:QDs at 290 K, i.e., 4 D and −100 Å^3, respectively, are significantly larger in magnitude than the above-mentioned values of $MAPbBr_3$ nanocrystals. However, a detailed comparison remains inconclusive because the $EA_{2\omega}$ spectra of $MAPbBr_3$ nanocrystals ($MAPbBr_3$:NC) were measured only at room temperature. To enable a more detailed comparison between $MAPbBr_3$:QDs and $MAPbBr_3$:NC, further measurements of the $EA_{2\omega}$ spectra of $MAPbBr_3$:NC at various T are necessary.

In contrast to $EA_{2\omega}$, the EA signals obtained from the F_{ap}−induced change in absorption intensity synchronized at the first harmonic of the modulation frequency, $EA_{1\omega}$, can be used to probe the electronic characteristics at the interfaces.[31,41−46] Usually, $EA_{1\omega}$ spectra are anticipated for an oriented ensemble system, yielding the spectra having the first derivative shape due to the linear Stark effect, which depends on $\Delta\boldsymbol{\mu}$. Contrary to such a conventional assumption, an intriguing deviation was observed in the $EA_{1\omega}$ spectra of the nanocrystalline film of methylammonium lead tri-iodide ($MAPbI_3$:NC): the $EA_{1\omega}$ spectra displayed second derivative-like shapes akin to those $EA_{2\omega}$ spectra, as we reported.[31] When the polarity of the F_{ap} was inverted, the positive and negative signals were inverted, though the shape was similarly second derivative-like. Based on the measurements of the $EA_{1\omega}$ spectra of $MAPbI_3$:NC at

https://doi.org/10.1021/acsaom.5c00441
ACS Appl. Opt. Mater. 2025, 3, 2870−2882

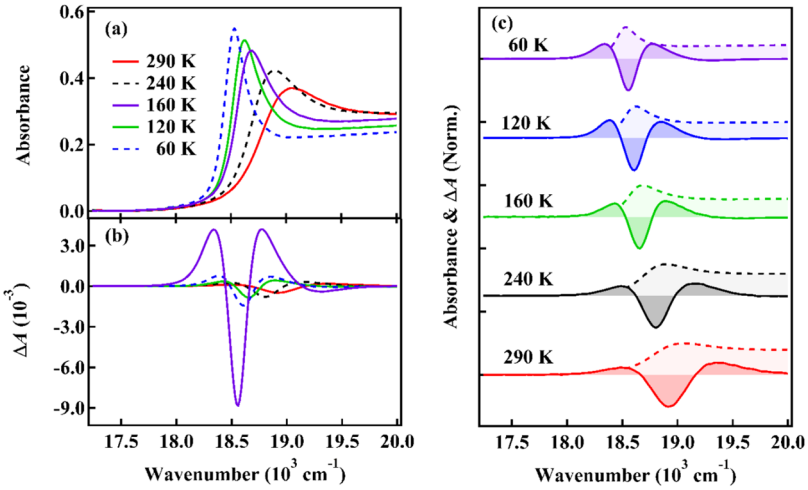

Figure 2. Absorption spectra (a) and $EA_{2\omega}$ spectra of $MAPbBr_3$:NC (Sample **A**) (b) at various temperatures in the range of 290−60 K. $EA_{2\omega}$ spectra were measured under F_{ap} of 0.3 $MVcm^{-1}$. Normalized absorption (broken line) and $EA_{2\omega}$ spectra (color shaded line) at different temperatures (c).

various T in the range of 290−60 K, we proposed that the peak position of the E_X band was slightly different at both interfaces of the perovskite film and that the F_{ap}−induced linear Stark shift to opposite energy direction on both interfaces, which resulted in the second derivative-like shape of the $EA_{1\omega}$ spectra. Further, the $EA_{1\omega}$ spectra of $MAPbI_3$:NC deposited on FTO with the PMMA overlayer were found to be very different from those deposited on the TiO_2 layer, indicating that the $EA_{1\omega}$ spectra are very sensitive to the interfaces of $MAPbI_3$:NC. The $EA_{1\omega}$ spectra of $MAPbI_3$:NC were also demonstrated to be strongly related to the roughness of the interfaces.[46]

Through those measurements of the $EA_{1\omega}$ spectra of $MAPbI_3$:NC, a question arises: how do the $EA_{1\omega}$ spectra of other halide perovskite films, particularly $MAPbBr_3$, respond under similar interfacial, temperature, and electric field conditions? In the present study, therefore, not only $EA_{2\omega}$ spectra but also $EA_{1\omega}$ spectra of the $MAPbBr_3$:NC film deposited on FTO and TiO_2 with the PMMA overlayer have been measured at various T in the range of 290−60 K, and the results are compared with those of $MAPbI_3$:NC to elucidate the influence of halide substitution from iodine to bromine. $MAPbI_3$, with its lower bandgap (∼1.55 eV), efficiently absorbs light in the visible range, making it ideal for solar cells, and undergoes a phase transition from tetragonal to orthorhombic while decreasing the temperature from room temperature. In contrast, the bromine substitution, i.e., $MAPbBr_3$, has a wider bandgap (∼2.3 eV), absorbing more in the green, blue, and UV regions, and does not show a phase transition, making it more suitable for LEDs, photodetectors, and tandem solar cells. The present study provides a comparative and mechanistic understanding of how halide substitution, which differs substantially in its crystal structure, excitonic properties, and interfacial responses to electric fields, tunes the excitonic Stark effect and interfacial properties. Understanding halide-dependent excitonic polarization and field coupling offers a fundamental basis for designing perovskite materials with improved electro-optic stability and device reliability.

EXPERIMENTAL METHODS

Sample Preparation

A compact TiO_2 layer was deposited by spin-casting titanium isopropoxide (TTIP) precursor solution (369 μL TTIP in 2.53 mL isopropyl alcohol (IPA) + 35 μL of 2 M HCl in 2.53 mL IPA) on the FTO substrates at 4000 rpm for 30 s. The FTO substrates with a TiO_2 layer were annealed at 100 °C for 10 min, followed by sintering at 400 °C for 1 h. The FTO substrates with and without a TiO_2 layer were transferred into a nitrogen-purged glovebox for subsequent deposition.

$MAPbBr_3$ films were spin-coated onto the substrates using a mixture of lead bromide ($PbBr_2$) and methylammonium bromide (MABr) in a 1:1 ratio dissolved in *n*-methyl-2 pyrrolidone (NMP). The solution was stirred at 70 °C until it became transparent. The precursor solution was spread over the substrates and spun with a rotor speed of 4000 rpm for 30 s. Immediately after spin coating, substrates coated with $MAPbBr_3$ solution were immersed upside down in anhydrous diethyl ether for 2 min to complete the crystallization process, followed by drying at room temperature (***R-T***). A PMMA film was subsequently deposited as an insulating layer on the top of the $MAPbBr_3$ film, and a semitransparent aluminum (Al) (∼15 nm) was deposited by thermal evaporation. The external electric field was applied between the FTO layer and Al film, which were used as front and back electrodes, respectively. Films' thicknesses ∼ 288 nm ($MAPbBr_3$) and ∼1 μm (PMMA) were measured using a profilometer (Veeco Dektak 150), which was used to estimate the applied electric field strength (applied electric field (F_{ap}) = applied voltage (V)/distance between electrodes (d), i.e., $F_{ap} = V/d$). Figure 1 shows the device structure for the second and first harmonic EA measurements, corresponding to the quadratic and linear EA spectra, respectively.

Optical Measurements

The absorption and electroabsorption (EA) spectra were measured using a laboratory-built system as described elsewhere.[24,25,45,46] Low temperature measurements were performed under vacuum conditions where samples were mounted in a cryostat (Daikin, V202C5LR) with a temperature (T)-controller (Scientific Inst., model 9600-1) equipped with a silicon diode thermometer. EA signals were recorded by detecting the field-induced change in transmitted light intensity from the sample (ΔT_{EX}) using a lock-in amplifier (SR830, SRS). Simultaneously, the transmitted light intensity (T_{EX}) was monitored without applied electric field to avoid the impact of Al/PMMA film. EA signals corresponding to the first harmonic ($EA_{1\omega}$) and second harmonic ($EA_{2\omega}$) of the modulation frequency were obtained from

https://doi.org/10.1021/acsaom.5c00441
ACS Appl. Opt. Mater. 2025, 3, 2870−2882

$\Delta A = -\frac{1}{\ln 10}\frac{\Delta T_{EX}}{T_{EX}}$ for $EA_{1\omega}$ and $\Delta A = -\frac{2\sqrt{2}}{\ln 10}\frac{\Delta T_{EX}}{T_{EX}}$ for $EA_{2\omega}$, respectively. Unless otherwise noted, the electric field was modulated with sinusoidal voltage at 1 kHz frequency in all of the measurements by using a function generator. This choice of frequency stems from our previous studies, which showed that the $EA_{2\omega}$ signal is strongly influenced by lower modulation frequencies (<500 Hz), due to the slow ion migration.[22] Hereafter, the applied field direction from the Al film to the FTO film is called as positive field direction (F_{ap}^{+}) (Figure 1b), while the opposite field direction, i.e., from the FTO film to the Al film, is called as negative field direction (F_{ap}^{-}) in the $EA_{1\omega}$ measurements.

RESULTS AND DISCUSSION

Measurements of Absorption and Second Harmonic Electroabsorption ($EA_{2\omega}$) Spectra

Optical measurements have been done for two kinds of samples, that is, the $MAPbBr_3$ nanocrystalline film ($MAPbBr_3$:NC) deposited on FTO and TiO_2 with the PMMA overlayer, respectively, which are hereafter referred to as Sample **A** and Sample **B**. The absorption and $EA_{2\omega}$ spectra of Sample **A** measured at various temperatures (T) ranging from 290 to 60 K, under an applied electric field strength (F_{ap}) of 0.3 $MVcm^{-1}$, are shown in Figure 2a,b, respectively. To better visualize spectral variations, normalized absorption and $EA_{2\omega}$ spectra are shown in Figure 2c. Corresponding spectra for Sample **B** under the same conditions are provided in the Supporting Information (SI, Figure S1).

The absorption spectra consist of a sharp exciton (E_X) band and a continuum band extending to shorter wavelengths. As the T decreases, the E_X absorption peak exhibits a pronounced red shift, indicating a narrowing of the bandgap. Similar T-dependent behavior was observed for $MAPbBr_3$:QDs and $MAPbI_3$ nanocrystalline film ($MAPbI_3$:NC).[24,25] This red shift of $MAPbBr_3$:NCs is attributed to lattice contraction and reduced thermal broadening at lower T. Unlike $MAPbI_3$:NC, which undergoes a tetragonal-to-orthorhombic phase transition alongside lattice contraction,[25] $MAPbBr_3$:NCs show only gradual lattice contraction without any structural phase change, as confirmed by T-dependent X-ray diffraction (Figure S2, SI). The Bragg peaks continuously shift to higher angles from 290 to 60 K, confirming this contraction. Notably, both samples exhibit nearly identical absorption spectra and T-dependent behavior (cf. Figures 2 and S1, SI).

The $EA_{2\omega}$ spectra show increased signal intensity with decreasing T, like the absorption spectra, as shown in Figures 2b and S1b of SI. Across all T, the $EA_{2\omega}$ spectra resemble the second derivative of a Gaussian profile, corresponding to the E_X band (Figures 2c and S1c). This behavior differs from $MAPbBr_3$:QDs, whose $EA_{2\omega}$ resembles the first derivative of a Gaussian profile.[24] As will be mentioned below, the first and second derivative shapes come from the change in polarizability ($\Delta\alpha$) and in electric dipole moment ($\Delta\mu$), respectively, following photoexcitation to the E_X band. These differences likely reflect variations in quantum confinement between the nanocrystalline film and quantum dots.

The T dependence of the absorption intensity normalized at 290 K and the intensity at the minimum of the $EA_{2\omega}$ spectra relative to the absorption, as shown in Figure 3, are essentially the same in both samples. It is also noted that the $EA_{2\omega}$ amplitude at 60 K is significantly larger than that at T above 100 K, likely due to reduced thermal broadening of the absorption spectrum. The F_{ap} dependence of the $EA_{2\omega}$ spectra

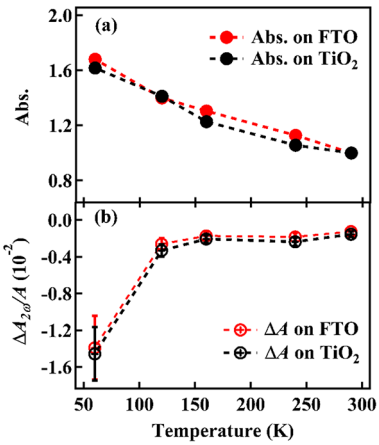

Figure 3. Temperature-dependent plots of the absorption intensity of the exciton peak (a) and $EA_{2\omega}$ intensity at the minimum relative to the absorbance at the exciton peak (b) of $MAPbBr_3$:NC in Sample **A** (red circle) and Sample **B** (black circle). The $EA_{2\omega}$ spectra were measured with F_{ap} of 0.3 $MVcm^{-1}$. The exciton peak intensities are normalized to the one at 290 K in both samples.

of Sample **A** observed at 290 and 60 K is shown in Figure 4, confirming that the signal magnitude varies quadratically with F_{ap}. Similar results for Sample **B** are shown in Figure S3 of SI. Thus, both samples exhibit identical $EA_{2\omega}$ spectra, indicating that the $EA_{2\omega}$ originates from the intrinsic quadratic Stark effect of $MAPbBr_3$:NC, which is subsequently utilized as the foundation to analyze the $EA_{2\omega}$ spectra. At 60 K, the $EA_{2\omega}$ spectra also display F_{ap}-dependent features in the higher energy continuum region, similar to $MAPbBr_3$:QDs. A zero-crossing point shifts to longer wavenumber (blue shift) as F_{ap} increases for both samples (Figure S4, SI). This F_{ap}-dependent oscillatory behavior in the continuum absorption region is attributed to Franz-Keldysh (F-K) oscillations,[47,48] consistent with similar phenomena observed in $EA_{1\omega}$ spectra, which will be shown later.

Analysis of $EA_{2\omega}$ Spectra to Determine $\Delta\mu$ and $\Delta\alpha$

The observed $EA_{2\omega}$ spectra were analyzed by ***I-M*** as described elsewhere, and the detailed information is given in SI, Note 1.[49−53] The $EA_{2\omega}$ analysis yields two key parameters: the change in electric dipole moment ($|\Delta\mu|$) and polarizability ($\Delta\bar{\alpha}$), which characterize the electronic response of the excitonic transition to F_{ap}. The parameter $|\Delta\mu|$ reflects the difference in permanent dipole moment between ground and excited states and is therefore sensitive to the charge separation or exciton localization. In contrast, $\Delta\bar{\alpha}$ represents the change in electronic polarizability upon excitation and indicates how readily the excited state electron cloud can be distorted by F_{ap}.

The simulated $EA_{2\omega}$ spectra of Sample **A** at 290 and 60 K are shown in Figure 5, and the other simulated spectra are shown in Figure S5 of SI. The values of $|\Delta\mu|$ and $\Delta\bar{\alpha}$ were estimated at each T for both Samples **A** and **B**, and the results are shown in Figure 6 and Table S1 (SI), along with the E_X peak positions and full width at half-maximum (FWHM) used for the simulation. At 290 K, $|\Delta\mu|$ and $\Delta\bar{\alpha}$ are estimated to be ∼2.7 D and ∼−14 $Å^3$, respectively, for both samples. As the T decreased from 290 to 120 K, $|\Delta\mu|$ remained nearly the same, and then exhibited a sharp increase at 60 K by more than twice (∼5.8 D). In contrast, $\Delta\bar{\alpha}$ in the present study at 290 K is −14 $Å^3$ and decreases with decreasing the T and becomes negligibly small (0.4 $Å^3$) at 60 K for both samples. The values of $|\Delta\mu|$ and

https://doi.org/10.1021/acsaom.5c00441
ACS Appl. Opt. Mater. 2025, 3, 2870−2882

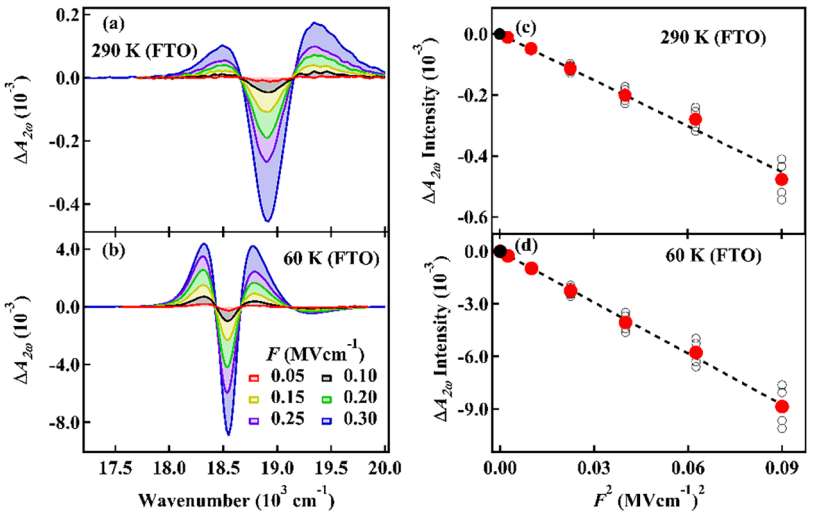

Figure 4. $EA_{2\omega}$ spectra of $MAPbBr_3$:NC (Sample **A**) at 290 K (a) and 60 K (b) under varying F_{ap} from 0.05 to 0.30 $MVcm^{-1}$. The plots of the $EA_{2\omega}$ intensity as a function of the square of F_{ap} are shown in panels (c, d), monitored at 18920 and 18550 cm^{-1}, respectively, which corresponds to the minimum of the spectra at 290 and 60 K.

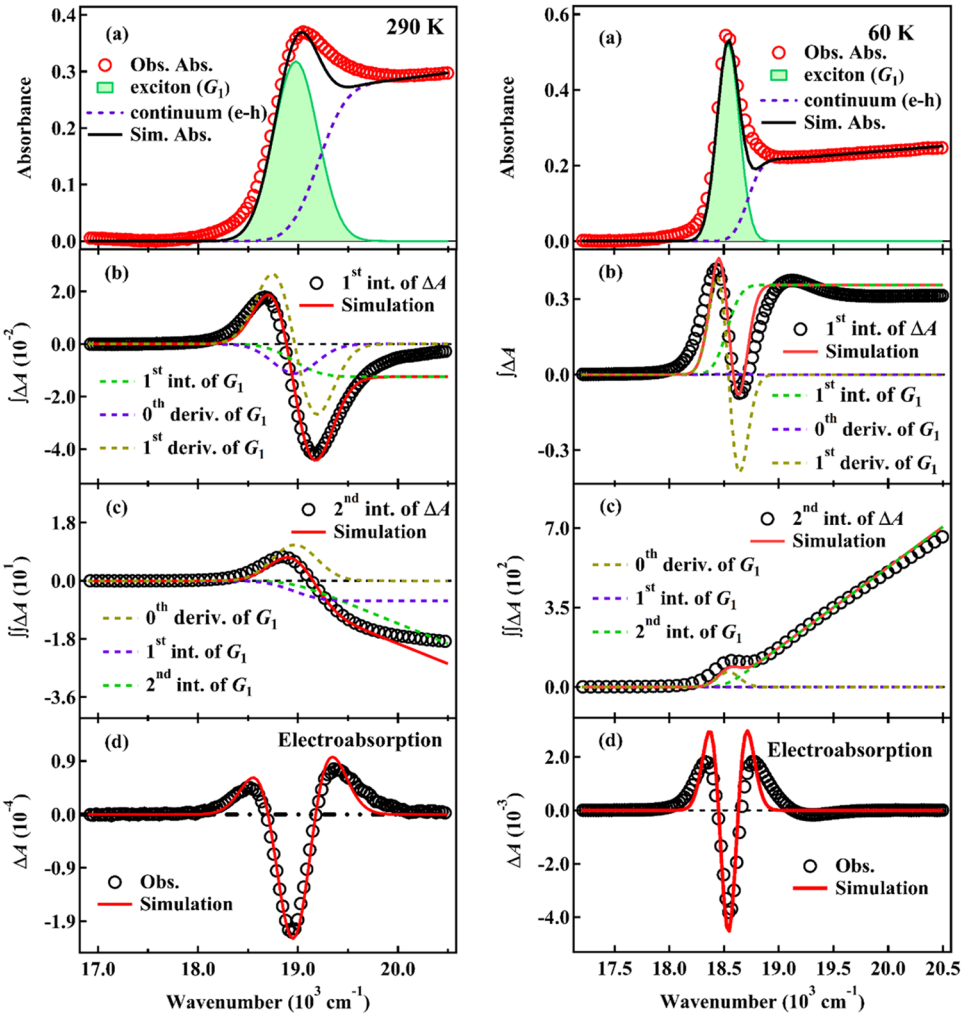

Figure 5. Analysis of the $EA_{2\omega}$ spectra of $MAPbBr_3$:NC (Sample **A**) at 290 K (left) and 60 K (right). Absorption spectra and their decomposition into exciton band (G_1) and continuum band (e−h), along with the sum of these bands (a). The first (b) and second (c) integrals of the $EA_{2\omega}$ spectra and their simulations were obtained using the derivatives and integrals of exciton band (G_1). (d) Observed $EA_{2\omega}$ spectra (black circle) and simulated spectra (red line). The contributions of the integral and derivative spectra of G_1 in each simulation are also shown in the figure.

https://doi.org/10.1021/acsaom.5c00441
ACS Appl. Opt. Mater. 2025, 3, 2870−2882

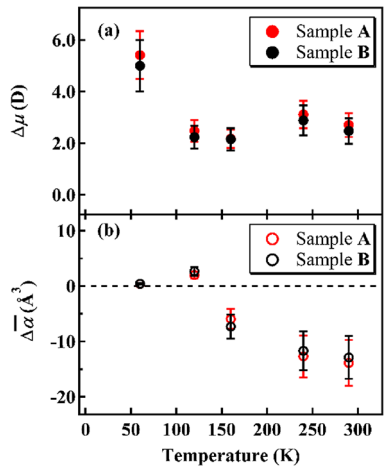

Figure 6. Magnitudes of $|\Delta\mu|$ (a) and $\Delta\bar{\alpha}$ (b) determined from the analysis of the $EA_{2\omega}$ spectra of Sample **A** (red circles) and Sample **B** (black circles) as a function of temperature.

$\Delta\bar{\alpha}$ at 290 K reported in our previous paper[22] are also given in Table S1 of SI. The previous value of $\Delta\bar{\alpha}$ at 290 K seems small beyond experimental error, but this may reflect differences in crystal size.

The observed trends can be interpreted in terms of the T-dependent lattice symmetry and dielectric properties of $MAPbBr_3$. As T decreases, the rotational motion of the MA^+ cation becomes restricted, leading to reduced lattice symmetry and a lower dielectric constant. The decrease in dielectric constant leads to weaker dielectric screening of the Coulomb interaction between electrons and holes, which increases their spatial correlation and promotes exciton localization. This enhanced localization produces a greater asymmetry in the charge distribution of the excitonic state, manifesting as the pronounced increase of $|\Delta\mu|$ at 60 K. Simultaneously, the reduced lattice symmetry and diminished electronic delocalization suppress the ability of the excitonic transition to polarize under F_{ap}, accounting for the marked reduction of $\Delta\bar{\alpha}$.

As reported previously, the magnitudes of $|\Delta\mu|$ and $\Delta\bar{\alpha}$ in $MAPbBr_3$:QDs were determined by using the same method with the present one to be ∼4 D and ∼−100 Å^3 at 290 K, which increased to ∼10 D and ∼−1070 Å^3 at 40 K, respectively. Thus, the magnitudes of $|\Delta\mu|$ and $\Delta\bar{\alpha}$ of $MAPbBr_3$:NC estimated in the present study are much smaller than the values in $MAPbBr_3$:QDs.[24] The large $\Delta\bar{\alpha}$ of $MAPbBr_3$:QDs explains why their $EA_{2\omega}$ spectra resemble the first derivative shape of the Gaussian profile of the E_X band, whereas $MAPbBr_3$:NCs in this study exhibit second derivative-like line shapes.

Estimation of Exciton Binding Energy of $MAPbBr_3$:NC

By assuming a Gaussian line shape for the spectral profile, the E_X absorption band can be separated from the continuum band contribution, which corresponds to the band-to-band transitions.[22,24,25] The detailed information is given in SI, Note 2. To reproduce the observed spectrum as a combination of E_X and continuum bands, FWHM and the center of the E_X band extracted from the analysis of $EA_{2\omega}$ spectra were employed (see Table S1). The simulations at 290 and 60 K are shown in Figure 7, and the fitting parameters are given in Table S1. The results at other T, i.e., 240, 160, 120 K, are shown in Figure S6 (SI). The present results indicate that the binding energy of the E_X of $MAPbBr_3$:NC (E_B) is nearly independent of T, which is ∼14 meV.

First Harmonic Electroabsorption ($EA_{1\omega}$) Spectra

The $EA_{1\omega}$ spectra of Samples **A** and **B** were measured at various T from 290 to 60 K under opposite field polarities, (F_{ap}^+ and F_{ap}^-) (see Figure 1b). The results obtained with F_{ap} of 0.3 MVcm^{-1} are shown in Figure 8. Both samples exhibit a strong polarity-dependence: reversing the direction of F_{ap} inverts the signal sign without altering its spectral shape at each T. This behavior is consistent with the $EA_{1\omega}$ spectra of $MAPbI_3$:NC, which we reported previously.[45] For F_{ap}^- (from FTO to Al), the $EA_{1\omega}$ spectra closely resemble the $EA_{2\omega}$ spectra at T above 120 K, indicating F_{ap}−induced broadening of the E_X absorption band. In contrast, when the direction of F_{ap} is reversed (from Al to FTO, F_{ap}^+), the $EA_{1\omega}$ spectra correspond to spectral narrowing of the E_X band.

At 60 K, the $EA_{1\omega}$ spectra of Sample **A** show a similar shape to the second derivative of the Gaussian profile, as seen at higher T, whereas Sample **B** exhibits a similar in shape to the first derivative. The origin of the different $EA_{1\omega}$ spectra of Sample **B** at 60 K will be discussed later. The F_{ap} dependences of the $EA_{1\omega}$ spectra at 290 and 60 K of both samples and the intensity monitored at the spectral maximum for F_{ap}^+ and minimum for F_{ap}^- are shown in Figure 9 for Sample **B** and Figure S7 for Sample **A**, confirming that the $EA_{1\omega}$ spectra result from the linear Stark effect.

As already mentioned, $EA_{2\omega}$ spectra are essentially the same in Samples **A** and **B** (see Figure 3). On the other hand, the $EA_{1\omega}$ intensity differs markedly between Samples **A** and **B**, indicating that the $EA_{1\omega}$ intensity is very sensitive to the

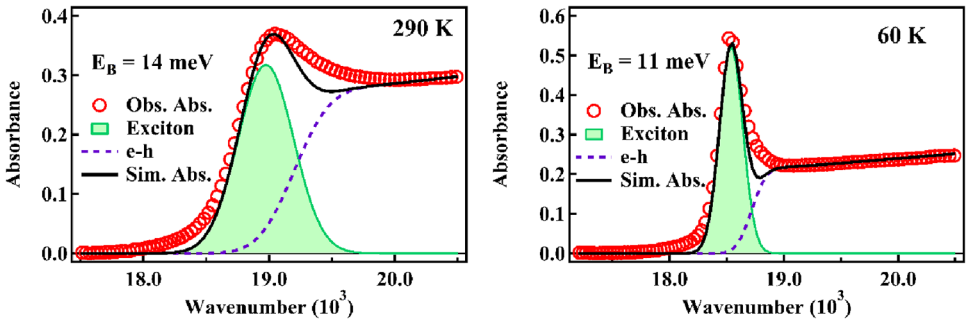

Figure 7. Estimation of the exciton binding energy (E_B). Experimentally obtained absorption spectra of the $MAPbBr_3$ nanocrystal (Sample **A**) at 290 K (left) and 60 K (right), together with simulated absorption spectra modeled as a sum of the excitonic and continuum (band-to-band) contributions. The corresponding exciton binding energies were derived from these simulations (see Note 2 of SI). Parameters used for the fitting are summarized in Table S1.

https://doi.org/10.1021/acsaom.5c00441
ACS Appl. Opt. Mater. 2025, 3, 2870−2882

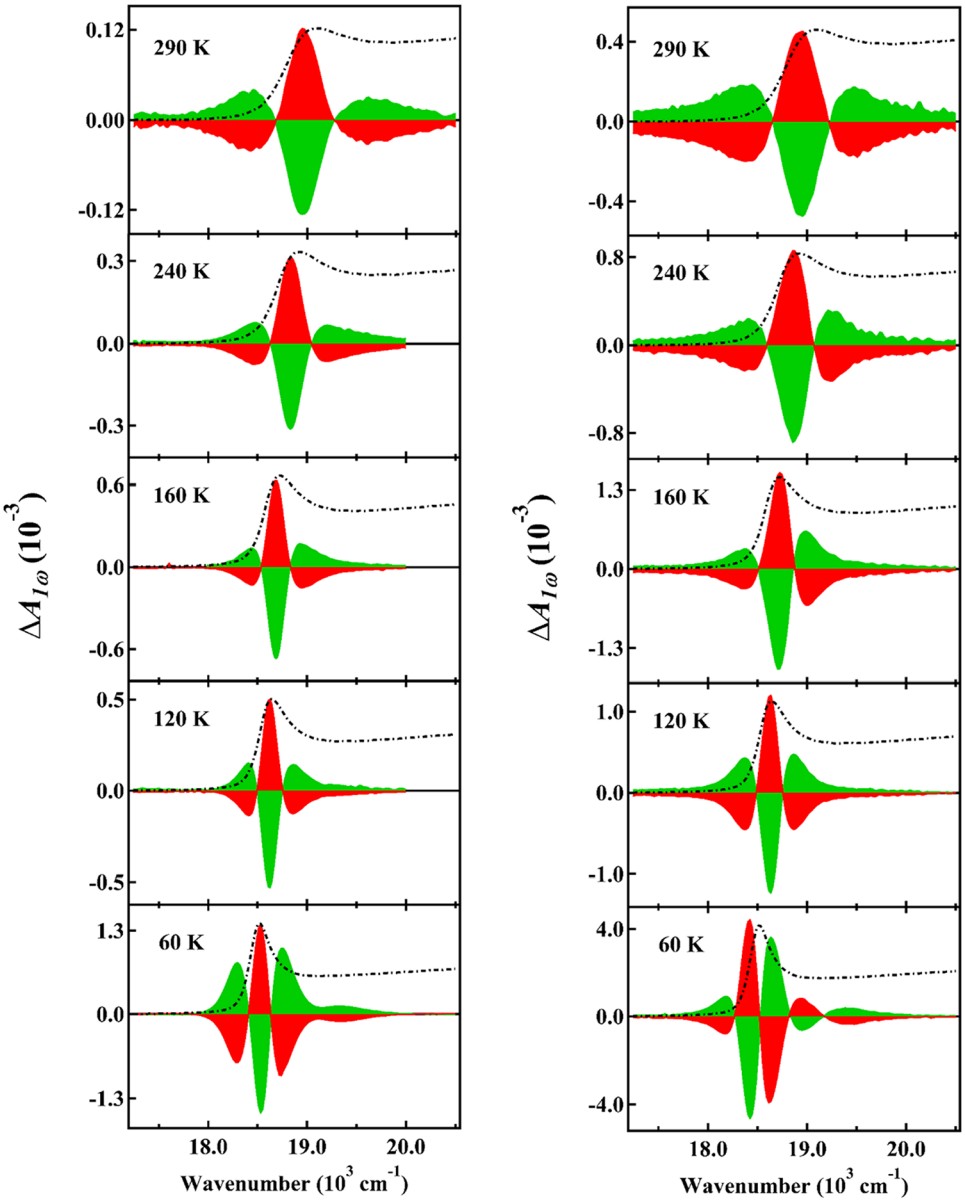

Figure 8. Absorption and $EA_{1\omega}$ spectra of Sample **A** (left) and Sample **B** (right) at different temperatures in the range of 290−60 K. The $EA_{1\omega}$ spectra were obtained with F_{ap} of 0.3 MVcm^{-1}. Spectra measured with the F_{ap}^{+} and F_{ap}^{-} are shown as red and green shaded lines, respectively. See Figure 1b for the field directions.

interface. As shown in Figure 10, both samples display a similar T dependence trend of $EA_{1\omega}$ intensities normalized to absorption intensity and a slight increase with decreasing T; however, Sample **A** exhibits approximately twice the intensity of Sample **B** across all measured T, highlighting the impact of the underlying substrate and interfacial dipole orientation.

In principle, the $EA_{1\omega}$ spectra stem from the F_{ap}−induced spectral shift induced by $\Delta\mu$, i.e., $-\Delta\mu F_{ap}$, which gives the first derivative shape of the absorption band in systems with uniformly oriented dipoles.[41−43] In randomly oriented ensembles, this effect is nullified by dipoles pointing in opposite directions from each other. However, $MAPbBr_3$:NC exhibits a second derivative-like $EA_{1\omega}$ spectra, as in the case of the $EA_{1\omega}$ spectra of $MAPbI_3$:NC reported previously.[31,45,46] This can be rationalized by considering the two interfaces bounding the $MAPbBr_3$:NC layer: the upper PMMA interface (interface 1) and the lower FTO or TiO_2 interface (interface 2), where the direction of $\Delta\mu$ at each interface is likely opposite, and the E_X absorption band associated with each interface exhibits slightly different peak energies. The energy separation between these two excitonic bands is defined as $\Delta\nu_{p-p}$ (peak-to-peak energy difference), arising from differences in local interfacial potential between $MAPbBr_3$:NC and the adjacent layers (PMMA and FTO/TiO_2). The F_{ap} − induced shift ($\Delta\nu$) corresponds to the Stark shift of the excitonic transition energies at interface 1 ($\Delta\nu_1$) and interface 2 ($\Delta\nu_2$) in opposite directions, directly proportional to $\Delta\mu{\cdot}F_{ap}$. The summed response of these oppositely shifted E_X bands yields a polarity-dependent second derivative-like $EA_{1\omega}$ spectra. The schematic representation of simulations based on two Gaussian E_X bands separated by $\Delta\nu_{p-p}$ and shifted by equal but opposite amounts ($\pm\Delta\nu_1$ and $\pm\Delta\nu_2$) successfully reproduce the observed profiles, as shown in Figure S8.

https://doi.org/10.1021/acsaom.5c00441
ACS Appl. Opt. Mater. 2025, 3, 2870−2882

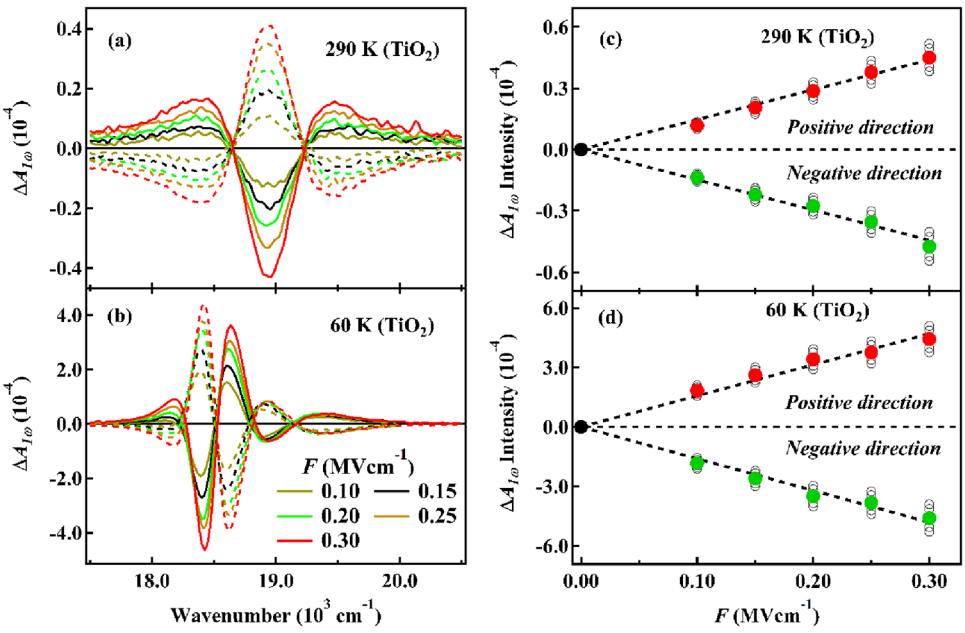

Figure 9. $EA_{1\omega}$ spectra of $MAPbBr_3$:NC (Sample **B**) at 290 K (a) and 60 K (b) under varying F_{ap} from 0.10 to 0.30 $MVcm^{-1}$. The plots of the $EA_{1\omega}$ intensity as a function of F_{ap} are shown in panels (c, d), monitored at 18920 and 18425 cm^{-1}, respectively, which corresponds to the maximum and minimum of the spectra at 290 and 60 K.

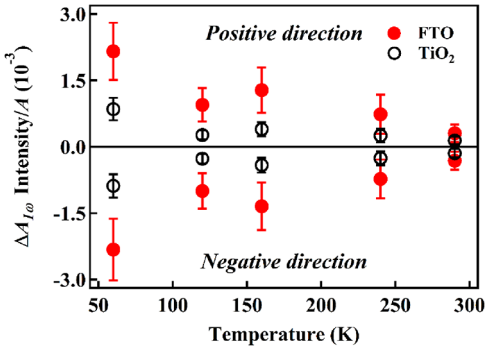

Figure 10. Plots of the $EA_{1\omega}$ signal intensity of Sample **A** (red circles) and Sample **B** (black circles) at the maximum (with F_{ap}^{+}) or minimum (with F_{ap}^{-}) relative to the absorbance at the exciton absorption peak, as a function of temperature.

The remarkable difference of the $EA_{1\omega}$ spectra of Samples **A** and **B** at 60 K clearly demonstrates that the $EA_{1\omega}$ spectra are very sensitive to the interface of $MAPbBr_3$:NC on the substrate (Figure 8). The polarity-dependent spectral broadening and narrowing of E_X absorption band induced by F_{ap} in $EA_{1\omega}$ spectra of Sample **A** at 290 and 60 K are simulated by assuming that two absorption bands with a Gaussian profile having different peak positions are shifted in opposite directions. The results are shown in Figure 11, where the energy separation of the two peaks (ν_{p-p}) is assumed to be 29.0 cm^{-1} at both T, and the F_{ap}−induced shift ($\Delta\nu$) is assumed to be 0.70 and 1.01 cm^{-1} at 290 and 60 K, respectively, in opposite directions at different interfaces. The magnitudes of the F_{ap}−induced shift of these bands into the opposite direction are assumed to be the same. The $EA_{1\omega}$ spectra of Sample **B** at 290 K are similarly simulated, as shown in Figure 12 (left), by assuming that ν_{p-p} is 11.70 cm^{-1} and $\Delta\nu$ is 0.70 cm^{-1} with opposite directions for absorption bands corresponding to different interfaces. The direction of $\Delta\mu$ is considered to be opposite to each other at both interfaces.

In the simulation of the $EA_{1\omega}$ spectra of Sample **B** at 60 K, the magnitude of the F_{ap}−induced shift is assumed to be different from each other for the two absorption bands corresponding to different interfaces, which may come from the difference in magnitude of $\Delta\mu$ on both interfaces. The results are shown in Figure 12 (right), where it is assumed that ν_{p-p} is 3.0 cm^{-1} and $\Delta\nu$ is 1.01 cm^{-1} on one interface and 1.15 cm^{-1} on another interface with opposite direction. The $EA_{1\omega}$ spectra rather similar to the first derivative of the Gaussian profile can be reproduced. These simulations confirm that the linear Stark effect originates primarily from the interfacial dipole difference. The stronger asymmetry and altered line shape in Sample **B** at 60 K suggest that the compact TiO_2 layer modifies the FTO surface and interfacial energetics,[54,55] influencing the field distribution and dipole orientation. The fitting parameters used in the simulation in Figures 11 and 12, i.e., ν_{p-p} and $\Delta\nu$, are shown in Table 1.

As already mentioned and shown in Figure S4 of SI, EA spectra showed zero-crossing points which depended on F_{ap} at 60 K. This observation was particularly pronounced in the $EA_{1\omega}$ spectra of Sample **B**, as shown in Figure 13. The zero-crossing points of the $EA_{2\omega}$ and $EA_{1\omega}$ signals observed at 60 K shift to the higher energy sides with increasing F_{ap} (see Figure 13). This phenomenon is consistent with Franz-Keldysh (F-K) oscillation arising from the field-band coupling in semiconductor materials.[47,48] In contrast, interference would not typically show such systematic F_{ap} dependence or energy shifts correlated with F_{ap} changes. Furthermore, the oscillations appear in the continuum absorption region above the excitonic peak and are reproducible across different sample interfaces, which supports their physical origin from the electronic band structure rather than experimental artifacts. The fact that the stronger F-K oscillation manifested more prominently in the $EA_{1\omega}$ spectra than in the $EA_{2\omega}$ spectra, especially in Sample **B**, probably indicates that the F-K oscillation dominantly results from the $MAPbBr_3$:NC in contact with the TiO_2, which may

https://doi.org/10.1021/acsaom.5c00441
ACS Appl. Opt. Mater. 2025, 3, 2870−2882

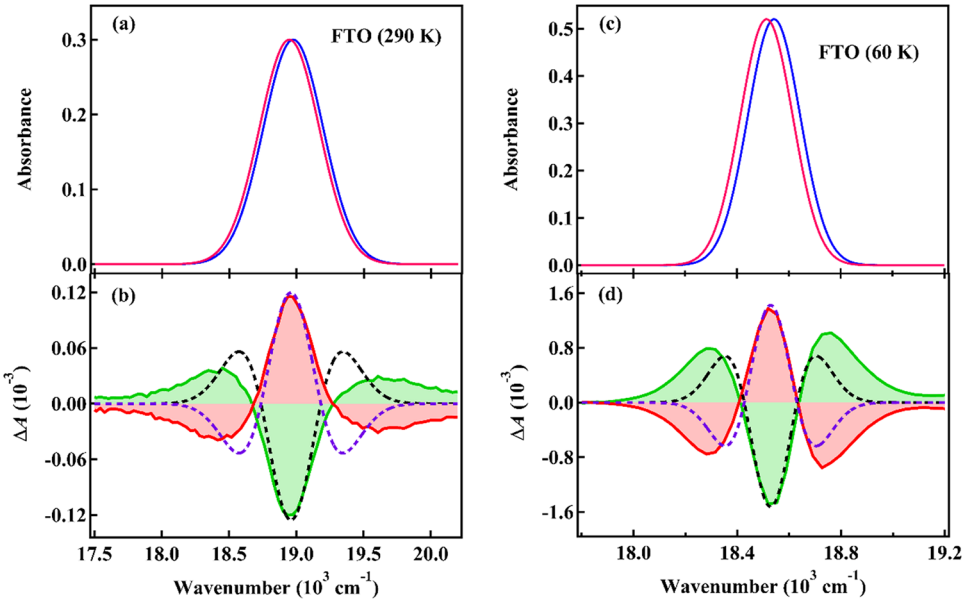

Figure 11. Simulated $EA_{1\omega}$ spectra of Sample **A** at 290 K (left) and 60 K (right) using the model shown in Figure S8 (SI). (a, c) Absorption spectra modeled with Gaussian profiles for the excitonic bands, having FWHM values of 520 cm^{-1} at 290 K and 240 cm^{-1} at 60 K. The absorption bands at the two interfaces are represented by red and blue Gaussian lines in panels (a, c) separated by a peak-to-peak energy difference ($\Delta\nu_{p-p}$). (b, d) Experimentally observed $EA_{1\omega}$ spectra measured under opposite field polarities, F_{ap}^{+} (red shaded line) and F_{ap}^{-} (green shaded line). The black and purple dashed lines represent the corresponding simulations, assuming an opposite field-induced spectral shift ($\Delta\nu$) in the mentioned bands of exciton peaks in opposite directions at the two interfaces. The values used for $\Delta\nu_{p-p}$ and $\Delta\nu$ at the two interfaces used in the simulations are given in Table 1 with experimental errors.

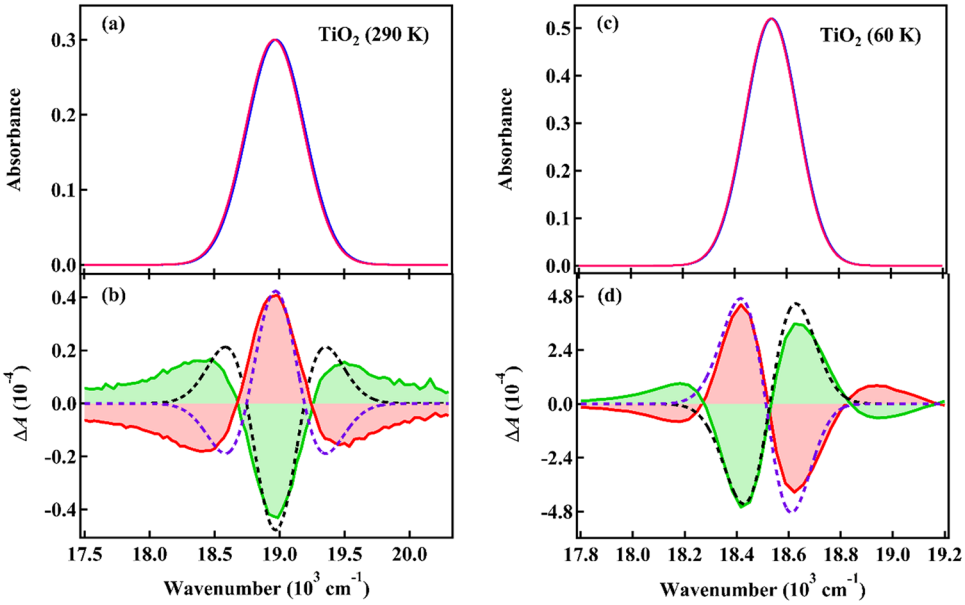

Figure 12. Simulated $EA_{1\omega}$ spectra of Sample **B** at 290 K (left) and 60 K (right) using the model shown in Figure S8 (SI). (a, c) Absorption spectra modeled with Gaussian profiles for the excitonic bands, having FWHM values of 520 cm^{-1} at 290 K and 240 cm^{-1} at 60 K. The absorption bands at the two interfaces are represented by red and blue Gaussian lines in panels (a, c) separated by a peak-to-peak energy difference ($\Delta\nu_{p-p}$). (b, d) Experimentally observed $EA_{1\omega}$ spectra measured under opposite field polarities, F_{ap}^{+} (red shaded line) and F_{ap}^{-} (green shaded line). The black and purple dashed lines represent the corresponding simulations, assuming an opposite field-induced spectral shift ($\Delta\nu$) in the mentioned bands of exciton peaks in opposite directions at the two interfaces. The values used for ν_{p-p} and $\Delta\nu$ used in the simulations are given in Table 1 with experimental errors.

generate enhanced local fields and reduced dielectric screening, strengthening band-to-band coupling under F_{ap}.

As reported in our previous papers,[31,45,46] $MAPbI_3$:NC also exhibits polarity-dependent $EA_{1\omega}$ spectra whose shapes resemble those of $EA_{2\omega}$ spectra, i.e., similar to the second derivative of a Gaussian function, and show a strong T dependence. This resemblance was attributed to the spectral broadening and narrowing of the E_X absorption band under F_{ap}^{+} and F_{ap}^{-}, respectively. Thus, the present $EA_{1\omega}$ spectra of $MAPbBr_3$:NC display similar polarity-dependent and derivative-like features. However, notable differences also exist

https://doi.org/10.1021/acsaom.5c00441
ACS Appl. Opt. Mater. 2025, 3, 2870−2882

Table 1. Parameters Used in Simulation of the $EA_{1\omega}$ Spectra Observed at 290 and 60 K for Sample A and Sample B (See Figures 11 and 12)[a]

	temperature (K)	$\Delta\nu_{p-p}$ (cm^{-1})	$\Delta\nu_1$ (cm^{-1})	$\Delta\nu_2$ (cm^{-1})
Sample **A**	290	29.0 (±2.0)	∓0.70 (±0.1)	±0.70 (±0.1)
	60	29.0 (±2.0)	∓1.01 (±0.1)	±1.01 (±0.1)
Sample **B**	290	11.7 (±1.0)	∓0.70 (±0.1)	±0.70 (±0.1)
	60	3.0 (±1.0)	∓1.01 (±0.1)	±1.15 (±0.05)

[a] $\Delta\nu_{p-p}$ denotes the energy separation between two peaks under zero field, and $\Delta\nu_1$ and $\Delta\nu_2$ are the field-induced shifts at interfaces 1 and 2, respectively. The shifts at both interfaces are considered to occur in opposite directions and depend on the polarity of F_{ap}.

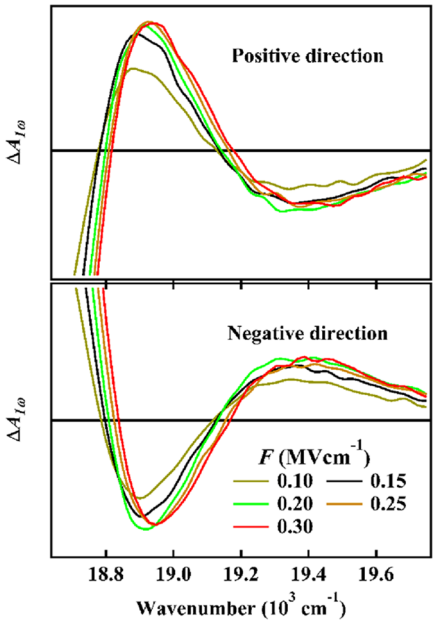

Figure 13. Extended view of the F_{ap} dependence of the $EA_{1\omega}$ spectra from 18650 to 19750 cm^{-1} of Sample **B** observed at 60 K in Sample **B**.

between $MAPbI_3$:NC and $MAPbBr_3$:NC, emphasizing the importance of comparing their $EA_{1\omega}$ spectra in detail.

The $EA_{1\omega}$ spectra of $MAPbI_3$:NC further clarify the role of structural phase and interface. The $MAPbI_3$:NC film on FTO (Sample **C**) and on TiO_2(Sample **D**) with the PMMA overlayer exhibited very different behavior from each other.[45] In Sample **D**, the $EA_{1\omega}$ signals were extremely weak at ***R-T***, but increased with decreasing ***T***. Further, the $EA_{1\omega}$ spectra of Sample **D** observed with F_{ap}^- (see Figure 1b) are similar in shape to the $EA_{2\omega}$ spectra, and positive and negative $EA_{1\omega}$ signals became opposite with F_{ap}^+ (see Figure 1b). Those results in Sample **D** are similar to the present ones of Samples **A** and **B** of $MAPbBr_3$:NC. In Sample **C**, on the other hand, the $EA_{1\omega}$ spectra similar to the $EA_{2\omega}$ spectra were observed with F_{ap}^+; that is, the $EA_{1\omega}$ spectra of Sample **C** observed above 200 K were opposite in signature to the $EA_{1\omega}$ spectra of Sample **D**. As the ***T*** decreased, the $EA_{1\omega}$ signal of Sample **C** became weaker, and inversion of the $EA_{1\omega}$ signal was found. Below ~200 K, both samples **C** and **D** show the $EA_{1\omega}$ spectra similar to the present $EA_{1\omega}$ spectra of $MAPbBr_3$:NC, including the spectral shape and polarity dependence. These variations in the $EA_{1\omega}$ spectra of $MAPbBr_3$:NC and $MAPbI_3$:NC may be attributed to the tetragonal to orthorhombic phase transition of $MAPbI_3$ below ~120 K, which alters lattice symmetry. In contrast, $MAPbBr_3$:NCs maintains a cubic phase across the full ***T*** range studied (290−60 K). Thus, while both systems ($MAPbI_3$:NC and $MAPbBr_3$:NC with different interfaces) exhibit polarity-dependent $EA_{1\omega}$ responses linked to interfacial dipole asymmetry, $MAPbBr_3$:NC demonstrates greater structural and electronic stability, an advantage for reproducible electro-optic performance.

In summary, the combined $EA_{1\omega}$ and $EA_{2\omega}$ analyses provide a unified understanding of the electro-optical behavior of $MAPbBr_3$ nanocrystalline films, revealing distinct interfacial and bulk contributions to their field response. The $EA_{1\omega}$ spectra, governed by the linear Stark effect, are highly sensitive to the orientation of the interfacial excitonic dipole. Their polarity-dependent and asymmetric spectral features between $MAPbBr_3$:NC deposited on FTO (Sample **A**) and on TiO_2 (Sample **B**) with the PMMA overlayer indicate opposite dipole alignments at the FTO (or TiO_2) and PMMA interfaces. These results establish $EA_{1\omega}$ as a sensitive probe of interfacial energetics, band alignment, and dipole orientation in perovskite heterostructures. In contrast, the $EA_{2\omega}$ spectra originate from the quadratic Stark effect, reflecting the intrinsic bulk excitonic response of $MAPbBr_3$:NC. Their identical behavior across both samples confirms their bulk origin. Overall, $EA_{1\omega}$ reflects interfacial field modulation, whereas $EA_{2\omega}$ captures the intrinsic bulk excitonic response. Together, they delineate how interfacial chemistry and lattice symmetry jointly govern the electro-optical properties of hybrid perovskites—insights that are essential for designing efficient, stable, and tunable perovskite-based modulators, detectors, and sensors.

CONCLUSIONS

Electroabsorption (EA) spectra of $MAPbBr_3$ nanocrystalline films ($MAPbBr_3$:NC) sandwiched between the FTO layer and the PMMA film and between the TiO_2 layer and the PMMA film were measured by synchronizing signals with the first ($EA_{1\omega}$) and second ($EA_{2\omega}$) harmonics of the applied sinusoidal field over 290−60 K. The $EA_{2\omega}$ spectra, attributed to the quadratic Stark effect, enabled quantitative estimation of the changes in dipole moment ($|\Delta\boldsymbol{\mu}|$) and average polarizability ($\Delta\bar{\alpha}$) of $MAPbBr_3$:NC following absorption at each temperature. In contrast, $EA_{1\omega}$ spectra exhibited spectral broadening and narrowing of the of E_X absorption band, which depended on field polarity. These effects were explained by the linear Stark effect of excitons located at the interfaces, with opposite spectral shifts arising from excitons in contact with PMMA and with FTO (or TiO_2). The interface-dependent nature of $EA_{1\omega}$ was further supported by simulations assuming slightly different exciton peak energies at the two boundaries. Additionally, Franz−Keldysh oscillations appeared in the continuum absorption region at 60 K, most clearly in $EA_{1\omega}$ spectra of films interfaced with TiO_2. This highlights the stronger interfacial contribution to field-induced modulation in such heterostructures. Overall, these results establish a clear distinction between bulk (quadratic Stark effect) and interfacial

https://doi.org/10.1021/acsaom.5c00441
ACS Appl. Opt. Mater. 2025, 3, 2870−2882

(linear Stark effect, F-K oscillations) contributions to the EA response of $MAPbBr_3$:NC films. Understanding these mechanisms provides valuable insights for designing perovskite-based optoelectronic devices such as electro-optic modulators, photodetectors, and field-sensitive sensors, where precise control of exciton-field interactions and interfacial effects is essential for optimizing performance and stability.

■ ASSOCIATED CONTENT

Supporting Information

The Supporting Information is available free of charge at https://pubs.acs.org/doi/10.1021/acsaom.5c00441.

Integral method analysis of $EA_{2\omega}$ spectra, estimation of binding energy from absorption spectra, absorption and $EA_{2\omega}$ spectra of the $MAPbBr_3$:NC film sandwiched between the TiO_2 layer and the PMMA film (Sample **B**), XRD pattern of the $MAPbBr_3$:NC film, applied field strength dependence of the $EA_{2\omega}$ spectra of Sample **B**, F-K oscillation in the $EA_{2\omega}$ spectra of the $MAPbBr_3$:NC film at 60 K, analysis of the $EA_{2\omega}$ spectra of $MAPbBr_3$:NC at 240, 160, and 120 K, estimation of the binding energy of exciton of $MAPbBr_3$:NC at 240, 160, and 120 K, applied field strength dependence of the $EA_{1\omega}$ spectra of Sample **A**, spectral broadening and narrowing of $\boldsymbol{E_X}$ absorption band as a result of the linear Stark effect, fitting parameters used for the analysis of the $EA_{2\omega}$ spectra and the magnitudes of $|\Delta\boldsymbol{\mu}|$, $\Delta\boldsymbol{\alpha}$, and binding energy of exciton (PDF)

■ AUTHOR INFORMATION

Corresponding Author

Nobuhiro Ohta − *Department of Applied Chemistry and Institute of Molecular Science, National Yang Ming Chiao Tung University, Hsinchu 300093, Taiwan; Center for Emergent Functional Matter Science, National Yang Ming Chiao Tung University, Hsinchu 300093, Taiwan;* orcid.org/0000-0003-4255-6448; Email: nohta@nycu.edu.tw

Authors

Shailesh Rana − *Department of Applied Chemistry and Institute of Molecular Science, National Yang Ming Chiao Tung University, Hsinchu 300093, Taiwan;* orcid.org/0000-0002-4349-101X

Kamlesh Awasthi − *Department of Applied Chemistry and Institute of Molecular Science, National Yang Ming Chiao Tung University, Hsinchu 300093, Taiwan; Center for Emergent Functional Matter Science, National Yang Ming Chiao Tung University, Hsinchu 300093, Taiwan;* orcid.org/0000-0001-7852-059X

Sudhakar Narra − *Department of Applied Chemistry and Institute of Molecular Science, National Yang Ming Chiao Tung University, Hsinchu 300093, Taiwan; Center for Emergent Functional Matter Science, National Yang Ming Chiao Tung University, Hsinchu 300093, Taiwan;* orcid.org/0000-0003-4893-9204

Eric Wei-Guang Diau − *Department of Applied Chemistry and Institute of Molecular Science, National Yang Ming Chiao Tung University, Hsinchu 300093, Taiwan; Center for Emergent Functional Matter Science, National Yang Ming Chiao Tung University, Hsinchu 300093, Taiwan;* orcid.org/0000-0001-6113-5679

Complete contact information is available at: https://pubs.acs.org/10.1021/acsaom.5c00441

Notes

The authors declare no competing financial interest.

■ ACKNOWLEDGMENTS

This work was supported by the National Science and Technology Council in Taiwan (NSTC 113-2113-M-A49-021, NSTC 114-2113-M-A49-013). This work was also supported by the Center for Emergent Functional Matter Science of National Yang Ming Chiao Tung University from The Featured Areas Research Center Program within the framework of the Higher Education Sprout Project by Ministry of Education in Taiwan.

■ REFERENCES

(1) Li, J.; Dagar, J.; Shargaieva, O.; Flatken, M. A.; Köbler, H.; Fenske, M.; Schultz, C.; Stegemann, B.; Just, J.; Többens, D. M.; et al. 20.8% Slot-Die Coated $MAPbI_3$ Perovskite Solar Cells by Optimal DMSO-Content and Age of 2-ME Based Precursor Inks. *Adv. Energy Mater.* **2021**, *11*, No. 2003460.

(2) Yoo, E. J.; Lyu, M.; Yun, J. H.; Kang, C. J.; Choi, Y. J.; Wang, L. Resistive Switching Behavior in Organic-Inorganic Hybrid $CH_3NH_3PbI_3$-XCl_x Perovskite for Resistive Random Access Memory Devices. *Adv. Mater.* **2015**, *27* (40), 6170−6175.

(3) Kim, Y. H.; Cho, H.; Heo, J. H.; Kim, T. S.; Myoung, N. S.; Lee, C. L.; Im, S. H.; Lee, T. W. Multicolored Organic/Inorganic Hybrid Perovskite Light-Emitting Diodes. *Adv. Mater.* **2015**, *27* (7), 1248−1254.

(4) Liang, F. X.; Jiang, J. J.; Zhao, Y. Z.; Zhang, Z. X.; Wu, D.; Zeng, L. H.; Tsang, Y. H.; Luo, L. B. Fabrication of MAPbBr3 Single Crystal p-n Photodiode and n-p-n Phototriode for Sensitive Light Detection Application. *Adv. Funct. Mater.* **2020**, *30* (32), No. 2001033.

(5) Jena, A. K.; Kulkarni, A.; Miyasaka, T. Halide Perovskite Photovoltaics: Background, Status, and Future Prospects. *Chem. Rev.* **2019**, *119* (5), 3036−3103.

(6) Li, B.; Hui, W.; Ran, X.; Xia, Y.; Xia, F.; Chao, L.; Chen, Y.; Huang, W. Metal Halide Perovskites for Resistive Switching Memory Devices and Artificial Synapses. *J. Mater. Chem. C* **2019**, *7* (25), 7476−7493.

(7) Yuan, H.; Debroye, E.; Janssen, K.; Naiki, H.; Steuwe, C.; Lu, G.; Moris, M.; Orgiu, E.; Uji-i, H.; De Schryver, F.; Samori, P.; Hofkens, J.; Roeffaers, M. Degradation of Methylammonium Lead Iodide Perovskite Structures through Light and Electron Beam Driven Ion Migration. *J. Phys. Chem. Lett.* **2016**, *7*, 561−566.

(8) Xiang, Y.; Zhang, F.; He, J.; Lian, J.; Zeng, P.; Song, J.; Qu, J. Light-Current Induced Acceleration of Degradation of Triethylammonium Lead Iodide Perovskite Solar Cells. *J. Power Sources* **2018**, *384*, 303−311.

(9) Nickel, N. H.; Lang, F.; Brus, V. V.; Shargaieva, O.; Rappich, J. Unraveling the Light-Induced Degradation Mechanisms of $CH_3NH_3PbI_3$ Perovskite Films. *Adv. Electron. Mater.* **2017**, *3*, No. 1700158.

(10) Gets, D. S.; Verkhogliadov, G. A.; Danilovskiy, E. Y.; Baranov, A. I.; Makarov, S. V.; Zakhidov, A. A. Dipolar Cation Accumulation at the Interfaces of Perovskite Light-Emitting Solar Cells. *J. Mater. Chem. C* **2020**, *8*, 16992−16999.

(11) Park, S. H.; Ahn, S.; Gwak, J.; Shin, K.; Ahn, S. K.; Yoon, K.; Cho, Y.; Kim, D. W.; Yun, J. H. Effectiveness of Full Spectrum Light Soaking on Solar Cell Degradation Analysis. *Curr. Appl. Phys.* **2013**, *13*, 1684−1688.

(12) Ren, F.; Lu, Q.; Meng, X.; Zhou, J.; Chen, R.; Wang, J.; Wang, H.; Liu, S.; Liu, Z.; Chen, W. Accelerating the Evaluation of Operational Lifetimes of Perovskite Solar Cells and Modules. *J. Energy Chem.* **2024**, *94*, 1−9.

(13) He, S.; Qiu, L.; Ono, L. K.; Qi, Y. How Far Are We from Attaining 10-Year Lifetime for Metal Halide Perovskite Solar Cells? *Mater. Sci. Eng., R* **2020**, *140*, No. 100545.
(14) Xu, F.; Zhang, T.; Li, G.; Zhao, Y. Mixed Cation Hybrid Lead Halide Perovskites with Enhanced Performance and Stability. *J. Mater. Chem. A* **2017**, *5*, 11450−11461.
(15) Zhu, H.; Pan, L.; Eickemeyer, F. T.; Hope, M. A.; Ouellette, O.; Alanazi, A. Q. M.; Gao, J.; Baumeler, T. P.; Li, X.; Wang, S.; Zakeeruddin, S. M.; Liu, Y.; Emsley, L.; Gratzel, M. Efficient and Stable Large Bandgap $MAPbBr_3$ Perovskite Solar Cell Attaining an Open Circuit Voltage of 1.65 V. *ACS Energy Lett.* **2022**, *7*, 1112−1119.
(16) Li, X.; Dar, M. I.; Yi, C.; Luo, J.; Tschumi, M.; Zakeeruddin, S. M.; Nazeeruddin, M. K.; Han, H.; Gratzel, M. Improved Performance and Stability of Perovskite Solar Cells by Crystal Crosslinking with Alkylphosphonic Acid ω-Ammonium Chlorides. *Nat. Chem.* **2015**, *7*, 703−711.
(17) Fu, Q.; Liu, H.; Tang, X.; Wang, R.; Chen, M.; Liu, Y. Multifunctional Two-Dimensional Polymers for Perovskite Solar Cells with Efficiency Exceeding 24%. *ACS Energy Lett.* **2022**, *7*, 1128−1136.
(18) Takahashi, S.; Uchida, S.; Jayaweera, P. V. V.; Kaneko, S.; Segawa, H. Impact of Compact TiO_2 Interface Modification on the Crystallinity of Perovskite Solar Cells. *Sci. Rep.* **2023**, *13*, No. 16068.
(19) Wang, X.; Liu, S.; Zhang, Z.; Pan, W.; Liang, H.; Wu, J.; Luo, J. Alkali Metal Fluoride for Efficient and Stable Planar TiO_2 Perovskite Solar Cells. *J. Mater. Chem. A* **2025**, *13*, 16929−16935.
(20) Huang, Y.; Hu, H.; Wang, R.; Zhou, S.; Du, J.; Yang, Y.; Bi, Z.; Chen, M.; Li, C. Internal Field and Interfaces in Organic and Perovskite Optoelectronic Devices Investigated via Electroabsorption Spectroscopy. *J. Mater. Chem. C* **2025**, *13*, 22104−22120.
(21) Ziffer, M. E.; Mohammed, J. C.; Ginger, D. S. Electroabsorption Spectroscopy Measurements of the Exciton Binding Energy, Electron-Hole Reduced Effective Mass, and Band Gap in the Perovskite $CH_3NH_3PbI_3$. *ACS Photonics* **2016**, *3*, 1060−1068.
(22) Awasthi, K.; Du, K. B.; Wang, C. Y.; Tsai, C. L.; Hamada, M.; Narra, S.; Diau, E. W. G.; Ohta, N. Electroabsorption Studies of Multicolored Lead Halide Perovskite Nanocrystalline Solid Films. *ACS Photonics* **2018**, *5*, 2408−2417.
(23) Ruf, F.; Magin, A.; Schultes, M.; Ahlswede, E.; Kalt, H.; Hetterich, M. Excitonic Nature of Optical Transitions in Electroabsorption Spectra of Perovskite Solar Cells. *Appl. Phys. Lett.* **2018**, *112*, No. 083902.
(24) Rana, S.; Awasthi, K.; Bhosale, S. S.; Diau, E. W. G.; Ohta, N. Temperature-Dependent Electroabsorption and Electrophotoluminescence and Exciton Binding Energy in $MAPbBr_3$ Perovskite Quantum Dots. *J. Phys. Chem. C* **2019**, *123*, 19927−19937.
(25) Hamada, M.; Rana, S.; Jokar, E.; Awasthi, K.; Diau, E. W.-G.; Ohta, N. Temperature-Dependent Electroabsorption Spectra and Exciton Binding Energy in a Perovskite $CH_3NH_3PbI_3$ Nanocrystalline Film. *ACS Appl. Energy Mater.* **2020**, *3*, 11830−11840.
(26) Kattoor, V.; Awasthi, K.; Jokar, E.; Diau, E. W. G.; Ohta, N. Integral Method Analysis of Electroabsorption Spectra and Electrophotoluminescence Study of $(C_4H_9NH_3)_2PbI_4$ Organic-Inorganic Quantum Well. *J. Phys. Chem. C* **2018**, *122* (46), 26623−26634.
(27) Amerling, E.; Baniya, S.; Lafalce, E.; Zhang, C.; Vardeny, Z. V.; Whittaker-Brooks, L. Electroabsorption Spectroscopy Studies of $(C_4H_9NH_3)_2PbI_4$ Organic-Inorganic Hybrid Perovskite Multiple Quantum Wells. *J. Phys. Chem. Lett.* **2017**, *8* (18), 4557−4564.
(28) Amerling, E.; Baniya, S.; Lafalce, E.; Blair, S.; Vardeny, Z. V.; Whittaker-Brooks, L. Quantifying Exciton Heterogeneities in Mixed-Phase Organometal Halide Multiple Quantum Wells via Stark Spectroscopy Studies. *ACS Appl. Mater. Interfaces* **2020**, *12* (47), 52538−52548.
(29) Walters, G.; Wei, M.; Voznyy, O.; Quintero-Bermudez, R.; Kiani, A.; Smilgies, D. M.; Munir, R.; Amassian, A.; Hoogland, S.; Sargent, E. The Quantum-Confined Stark Effect in Layered Hybrid Perovskites Mediated by Orientational Polarizability of Confined Dipoles. *Nat. Commun.* **2018**, *9*, No. 4214.
(30) Li, C.; Tscheuschner, S.; Paulus, F.; Hopkinson, P. E.; Kießling, J.; Köhler, A.; Vaynzof, Y.; Huettner, S. Iodine Migration and Its Effect on Hysteresis in Perovskite Solar Cells. *Adv. Mater.* **2016**, *28* (12), 2446−2454.
(31) Awasthi, K.; Kala, K.; Rana, S.; Diau, E. W.-G.; Ohta, N. Switching between Spectral Broadening and Narrowing of the Exciton Absorption Band of a $CH_3NH_3PbI_3$ Film on Altering the Polarity of an Applied Electric Field. *Appl. Phys. Lett.* **2020**, *116*, No. 251101.
(32) Tanaka, K.; Sano, F.; Takahashi, T.; Kondo, T.; Ito, R.; Ema, K. Two-Dimensional Wannier Excitons in a Layered-Perovskite-Type Crystal $(C_6H_{13}NH_3)_2PbI_4$. *Solid State Commun.* **2002**, *122* (5), 249−252.
(33) Amerling, E.; Hansen, K. R.; Whittaker-Brooks, L. Resolving Buried Optoelectronic Features in Metal Halide Perovskites via Modulation Spectroscopy Studies. *J. Mater. Chem. A* **2021**, *9* (42), 23746−23764.
(34) Xing, Z.; Zang, Z.; Li, H.; Ning, Z.; Wong, K. S.; Chow, P. C. Y. Improved Structural Order and Exciton Delocalization in High-Member Quasi-Two-Dimensional Tin Halide Perovskite Revealed by Electroabsorption Spectroscopy. *J. Phys. Chem. Lett.* **2023**, *14*, 4349−4356.
(35) Paraecattil, A. A.; De Jonghe-Risse, J.; Pranculis, V.; Teuscher, J.; Moser, J. E. Dynamics of Photocarrier Separation in $MAPbI_3$ Perovskite Multigrain Films under a Quasistatic Electric Field. *J. Phys. Chem. C* **2016**, *120*, 19595−19602.
(36) Guo, Y.; Jia, Y.; Li, N.; Chen, M.; Hu, S.; Liu, C.; Zhao, N. Degradation Mechanism of Perovskite Light-Emitting Diodes: An In Situ Investigation via Electroabsorption Spectroscopy and Device Modelling. *Adv. Funct. Mater.* **2020**, *30*, No. 1910464.
(37) Kim, H.; Zhao, L.; Price, J. S.; Grede, A. J.; Roh, K.; Brigeman, A. N.; Lopez, M.; Rand, B. P.; Giebink, N. C. Hybrid Perovskite Light Emitting Diodes under Intense Electrical Excitation. *Nat. Commun.* **2018**, *9*, No. 4893.
(38) Hong, X.; Ishihara, T.; Nurmikko, A. V. Dielectric Confinement Effect on Excitons in PbI_4-Based Layered Semiconductors. *Phys. Rev. B* **1992**, *45* (12), 6961−6964.
(39) Rana, S.; Awasthi, K.; Diau, E. W. G.; Ohta, N. Illumination Power-Dependent Electroabsorption of Excitons in a $CH_3NH_3PbI_3$ Perovskite Film. *J. Phys. Chem. C* **2021**, *125*, 27631−27637.
(40) Ruf, F.; Rietz, P.; Ayguler, M. F.; Kelz, I.; Docampo, P.; Kalt, H.; Hetterich, M. The Bandgap as a Moving Target: Reversible Bandgap Instabilities in Multiple-Cation Mixed-Halide Perovskite Solar Cells. *ACS Energy Lett.* **2018**, *3*, 2995−3001.
(41) Ohta, N.; Okazaki, S.; Yamazaki, I. Stark Shift in Absorption Spectra of Langmuir-Blodgett Mixed Monolayer Films New Finding of a Complex Formation of Chromophoric Oxacyanine. *Chem. Phys. Lett.* **1994**, *229*, 394−400.
(42) Roiati, V.; Mosconi, E.; Listorti, A.; Colella, S.; Gigli, G.; De Angelis, F. Stark Effect in Perovskite/TiO_2 Solar Cells: Evidence of Local Interfacial Order. *Nano Lett.* **2014**, *14* (4), 2168−2174.
(43) Cappel, U. B.; Feldt, S. M.; Schoneboom, J.; Hagfeldt, A.; Boschloo, G. The Influence of Local Electric Fields on Photoinduced Absorption in Dye-Sensitized Solar Cells. *J. Am. Chem. Soc.* **2010**, *132* (26), 9096−9101.
(44) Ponomarev, I. V.; Deych, L. I.; Lisyansky, A. A. Electric-Field-Induced Narrowing of Exciton Linewidth. *Phys. Rev. B* **2005**, *72* (11), No. 115304.
(45) Rana, S.; Awasthi, K.; Diau, E. W.-G.; Ohta, N. Interface- and Temperature-Sensitive Linear Electric Field Effects on Exciton Absorption of $CH_3NH_3PbI_3$ Perovskite Films. *J. Phys. Chem. C* **2023**, *127*, 24383−24392.
(46) Narra, S.; Chung, Y.-L.; Rana, S.; Rajamanickam, P.; Awasthi, K.; Diau, E. W.-G.; Ohta, N. Surface Roughness Dependent Linear Electric Field Effects on the Exciton Absorption of Methylammonium Lead Triiodide Perovskite Films. *J. Phys. Chem. C* **2024**, *128* (40), 17134−17140.
(47) Hamakawa, Y.; Germano, F. A.; Handler, P. Interband Electro-Optical Properties of Germanium. I. Electroabsorption. *Phys. Rev.* **1968**, *167*, 703−709.

https://doi.org/10.1021/acsaom.5c00441
ACS Appl. Opt. Mater. 2025, 3, 2870−2882

(48) Miller, D. A. B.; Chemla, D. S.; Schmitt-Rink, S. Relation between Electroabsorption in Bulk Semiconductors and in Quantum Wells: The Quantum-Confined Franz-Keldysh Effect. *Phys. Rev. B* **1986**, *33*, 6976−6982.
(49) Liptay, W. Dipole Moments and Polarizabilities of Molecules in Excited Electronic States. In *Excited States*; Lim, E. C., Ed.; Academic Press: New York, 1974; Vol. *1*, pp 129−229.
(50) Locknar, S. A.; Peteanu, L. A. Investigation of the Relationship between Dipolar Properties and Cis-Trans Configuration in Retinal Polyenes: A Comparative Study Using Stark Spectroscopy and Semiempirical Calculations. *J. Phys. Chem. B* **1998**, *102* (21), 4240−4246.
(51) Bublitz, G. U.; Boxer, S. G. Stark Spectroscopy: Applications in Chemistry, Biology, and Materials Science. *Annu. Rev. Phys. Chem.* **1997**, *48* (1), 213−242.
(52) Jalviste, E.; Ohta, N. Theoretical Foundation of Electroabsorption Spectroscopy: Self-Contained Derivation of the Basic Equations with the Direction Cosine Method and the Euler Angle Method. *J. Photochem. Photobiol., C* **2007**, *8* (1), 30−46.
(53) Awasthi, K.; Iimori, T.; Ohta, N. Integral Method Analysis of Electroabsorption Spectra and Its Application to Quantum Dots of PbSe. *J. Phys. Chem. C* **2014**, *118* (31), 18170−18176.
(54) Wang, X.; Fang, Y.; He, L.; Wang, Q.; Wu, T. Influence of Compact TiO_2 Layer on the Photovoltaic Characteristics of the Organometal Halide Perovskite-Based Solar Cells. *Mater. Sci. Semicond. Process.* **2014**, *27*, 569−576.
(55) Sławek, A.; Starowicz, Z.; Lipinski, M. The Influence of the Thickness of Compact TiO_2 Electron Transport Layer on the Performance of Planar $CH_3NH_3PbI_3$ Perovskite Solar Cells. *Materials* **2021**, *14*, 3295.

https://doi.org/10.1021/acsaom.5c00441
ACS Appl. Opt. Mater. 2025, 3, 2870−2882